

Petra Foerst^{1,*}
Sebastian Gruber¹
Michael Schulz²
Nicole Vorhauer³
Evangelos Tsotsas³

Characterization of Lyophilization of Frozen Bulky Solids

Two methods to study the primary freeze-drying behavior of bulky solids are presented, namely, lyomicroscopy and neutron imaging. The applicability of both methods to visualize the evolution of the sublimation front is tested for maltodextrin particles with different sizes and solid concentrations. Exemplary results for both methods are reported and the applicability of both methods to study freeze-drying behavior of bulk solids is described. To estimate the impact of particle size and bed height for the freeze-drying of bulky solids, a modified Biot number is introduced to estimate the optimum particle size for a given bed height and formulation. The applicability of the two methods with regard to the modified Biot numbers is discussed.

 This is an open access article under the terms of the Creative Commons Attribution-NonCommercial License, which permits use, distribution and reproduction in any medium, provided the original work is properly cited and is not used for commercial purposes.

Keywords: Biot number, Bulk solids, Limiting particle size, Lyomicroscopy, Neutron imaging

Received: September 13, 2019; *revised:* February 20, 2020; *accepted:* February 21, 2020

DOI: 10.1002/ceat.201900500

1 Introduction

Lyophilization or freeze-drying is commonly applied since many years to stabilize (bio-)pharmaceutical substances and high-value foods for long-term storage. Even though it is an industrially established technique, the impact of the pore structure on mass transport through the porous structure and final product quality is still an actual subject of research [1–3]. Especially the drying behavior of particle beds is not yet fully understood [4]. Two cases are distinguished: lyophilization of solutions in vials or other containers (Fig. 1a) and frozen particulate matter (Figs. 1b, c). The process is carried out in frozen state of the product and below the triple point of the solvent. For amorphous substances such as amorphous sugars, the temperature of the maximally freeze-concentrated solution $T_g^{(1)}$ is the decisive maximum product temperature [5].

During primary drying, the solvent (in dark gray in Fig. 1) is removed by sublimation. The evaporated solvent is then transported through the porous dry part of the sample (in light gray in Fig. 1). Most commonly, the latent heat of sublimation is supplied by a heated shelf at the bottom of the sample [5]. In the theoretical description of freeze-drying of solutions, it is assumed that a planar drying front evolves at the open surface of the frozen solution and then travels to the bottom (Fig. 1a).

For particulate substances such as fruits, frozen starter cultures, or spray-frozen particles, the freeze-drying behavior is much less well understood. Only a few models exist so far to predict the freeze-drying behavior of particulate substances [6–8].

For the evolution of the sublimation front in particulate solids, different model assumptions exist. Trelea et al. [6] devel-

oped a model applicable to starter culture pellets in a size range of several millimeters. They assumed that the mass transfer resistance lies in the pellets and the outer mass transfer resistance in the bed is neglected. Therefore, a radial sublimation front evolves in each pellet and the sublimation rate strongly decreases when the sublimation front recedes within the particle (Fig. 1c).

The model assumptions by Trelea et al. [6] are quite different to the model proposed by Liapis and Bruttini [7]. They developed a model for spray-frozen pharmaceutical powders in a much smaller size range (particle size $< 20 \mu\text{m}$). Due to the small size of the particles, the heat and mass transfer resistance inside the particles is neglected and only the voids between the particles are considered. Their simulation yielded a sharp main sublimation front moving from the top to the bottom of the particle bed and a small front evolving after 8 h from the bottom to the top of the sample.

Chitu et al. [8] modeled the freeze-drying of spray-frozen small particles (particle size $\approx 100 \mu\text{m}$) by an advancing phase-change approach. According to this approach, due to the porous (permeable) nature of the particle bed, the main drying front started from the bottom of the bed, and the sublimation

¹Prof. Dr.-Ing. Petra Foerst, Sebastian Gruber

petra.foerst@tum.de

Process Systems Engineering, TU Munich, Gregor-Mendel-Strasse 4, 85354 Freising, Germany.

²Dr. Michael Schulz

Research Neutron Source Heinz Maier-Leibnitz, TU Munich, Lichtenbergstrasse 1, 85748 Garching, Germany.

³Dr.-Ing. Nicole Vorhauer, Prof. Dr.-Ing. Evangelos Tsotsas

Chair of Thermal Process Engineering, Otto-von-Guericke-University, Universitaetsplatz 2, 39106 Magdeburg, Germany.

1) List of symbols at the end of the paper.

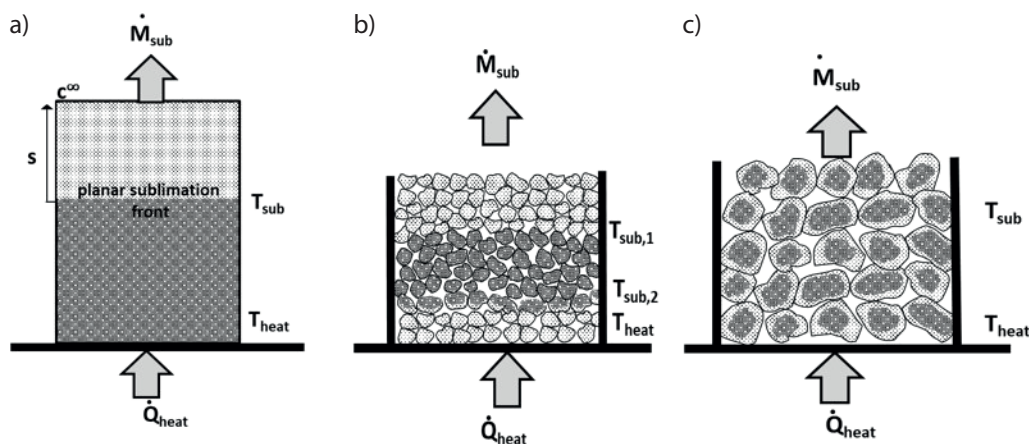


Figure 1. Schematic illustration of basic model assumptions for lyophilization of solutions and particulate solids [2]. Dark gray: frozen region; light gray: dried porous region. (a) Solution; (b) fixed particle bed with two planar drying fronts; (c) fixed particle bed with drying fronts evolving within each particle as suggested by Trelea et al. [6]. Notice that vial and particles are initially fully saturated with ice, while the interparticle space (in white) is initially free of ice. T_{sub} , temperature at the sublimation front; T_{heat} , temperature of the heating plate; \dot{M}_{sub} , sublimed water vapor; \dot{Q}_{heat} , heat flow provided by the lower plate.

rates were mainly controlled by the heat conduction through the formed dried layer (Fig. 1b).

However, a direct experimental validation for the different models is still missing. Furthermore, no direct observation of the sublimation front exists so far. Especially the role of particle size on freeze-drying behavior is not well understood. No comprehensive model for a large range of particle sizes and no limiting particle size for the applicability of the existing models are available. Furthermore, the impact of the ratio of inner to outer porosity and pore size is not understood.

Therefore, it is the aim of the paper to present two different methods to study freeze-drying behavior in situ and to visualize sublimation fronts of particle beds, namely, by lyomicroscopy and neutron imaging. The lyomicroscopy is a light microscopic technique where the sublimation front can be assessed two-dimensionally under defined conditions [10–12]. Neutron imaging is a powerful technique to visualize drying fronts in convective drying since neutrons are very sensitive to water [13, 14]. Recently, it has been shown that sublimation fronts in packed particle beds during freeze-drying can also be visualized by neutron imaging [9]. Both techniques will be described for their application to study the freeze-drying behavior of particle beds and their advantages and disadvantages will be discussed. In addition, a modified Biot number for the mass transport in particle beds is introduced. The dimensionless Biot number should help to decide whether the main mass transport limitation is inside the particles or in the particle bed, and to identify suitable particle sizes and/or bed heights for the given process.

2 Materials and Methods

2.1 Materials

Maltodextrin (Glucidex 12D, Roquette, France) was used as a model substance. Two different solid concentrations were tested ($c = 0.05$ and 0.2 (w/w)). For the lyomicroscopic measurements, the solutions were prepared with ultrapure water (filtered with Millipak[®] Express 40 Filter; Merck, Germany). The solutions for the neutron imaging were prepared with D₂O (99.9 % D; VWR Chemicals, USA) due to the high attenuation coefficients of water for neutrons.

2.2 Particle Generation

For the study of packed particle beds, frozen particles were prepared. For the neutron imaging experiments, two different particle sizes were produced. Particles were generated by spray-freezing of the solution with an ultrasonic nozzle (narrow spray atomizer nozzle; sonaer ultrasonics, USA). The particle size was adjusted by both ultrasound intensity and the flow rate through the nozzle. The flow rate was adjusted with an injection pump (Standard Infuse Pump 11 Elite, Harvard Apparatus, Canada).

For neutron imaging, large particles with a size of 3.55 mm were produced by switching the ultrasound off and dropping the solution with a low rate of 2.5 mL min^{-1} driven by gravitation into liquid nitrogen. Small particles with a size of $70 \mu\text{m}$ were generated with a 40 % ultrasound intensity and a flow rate of 5 mL min^{-1} . For lyomicroscopy, two particle sizes were produced in the range of 70 – $140 \mu\text{m}$. Larger particles were not made due to the limited size of the sample chamber. The 70 - μm particles were generated with 51 % ultrasound intensity and 4 mL min^{-1} flow rate. The 140 - μm particles were created with 20 mL min^{-1} and 11 % ultrasound intensity. The particles were stored at $-80 \text{ }^\circ\text{C}$ until use.

2.3 Lyomicroscopy

2.3.1 Sample Slicing

In lyomicroscopy, a thin slice of the sample was placed in the microscope in frozen state in a thin slice (schematic drawing in Fig. 2a). To be able to visualize drying fronts in particle packings, particle beds were cut into thin slices. Before cutting, the frozen particles were compacted with a pressure of 109 kPa for 24 h at -20°C and then stored at -80°C until use. The slices were prepared with a cryotome (CryoStar HM 560 MV; Microm GmbH, Germany). The samples were frozen with Cryogel (Leica, Germany) at -45°C to the sample holder. Both the sample and the knife (Microtom Blades DB80; Leica, Germany) were cooled to -20°C . The thickness of the slices was $50\ \mu\text{m}$. The cooled sample was placed between a precooled quartz crucible and a precooled cover slip and placed into the cool-stage of the microscope. The placement of the sample as well as a picture of the slice are given in Figs. 2a and b.

2.3.2 Freeze-Drying Runs

The experimental setup for the visualization of the sublimation front in the lyomicroscope is displayed in Fig. 2c. An evacuable cool-stage specifically designed for freeze-drying (FDSC196 Linkam, UK) was placed on the object table of a light microscope (BX51; Olympus, Germany). The pressure in the cool-

stage was adjusted with a vacuum pump (E2M1.5; Edwards, Germany) and controlled with a pressure controller (CVC 3000; Vacuubrand, Germany). The temperature in the cool-stage was controlled by an electrical heating block and liquid nitrogen. The pictures were recorded with a camera (PL-A662; Pixelink, USA). For a controlled drying temperature ramps could be programmed within the software LinkSys 32 (Linkam, UK).

After placing the sample onto the heating block of the cool stage (Fig. 2a), the sample was frozen to -30°C with a defined cooling rate of $20\ \text{K}\ \text{min}^{-1}$ and further to -50°C with a cooling rate of $5\ \text{K}\ \text{min}^{-1}$. After freezing and a holding time of 5 min, the cool-stage was evacuated to a pressure of $(10 \pm 3)\ \text{Pa}$. The sublimation process was started by heating the sample again with a rate of $2\ \text{K}\ \text{min}^{-1}$ to -42°C and pictures were taken every 30 s. The sublimation front inside the particles was observed with transmitted light with a magnification factor of 100 for the large and 200 for the small particles. For the observation of the sublimation front through the particle bed, a magnification of 50 was chosen.

The sublimation front becomes visible by a step change in light transmittance. The dried region appears darker than the frozen region due to stronger scattering in the dried region. The drying front was assessed manually by a polygon tool within the software Linksys 32 (Linkam, UK). With this tool, the area of the frozen fraction is obtained. From the area of the frozen fraction, the equivalent diameter x_{pm} (diameter of a circle with same frozen area) was evaluated.

2.4 Neutron Imaging

The neutron imaging facility ANTARES [15, 16] is located at the cold neutron source of the FRM II reactor at Heinz Maier-Leibnitz Zentrum, Garching, Germany. The experimental procedure for the neutron imaging experiments is described in [4]. Neutron imaging offers good contrast for hydrogen and deuterium while providing good penetration for aluminum. Therefore, the freeze-drying cell was constructed of aluminum [17]. The effective spatial resolution of the setup was estimated to be $\approx 100\ \mu\text{m}$. The sample was placed in a container as described below in a standard FRM II closed cycle cryostat.

To prepare the setup, particles were prefilled in a custom-built vacuum cell shown in the photograph in Fig. 3b. The setup of the cell is described in [17]. Briefly, a small circular freeze-drying cell made from aluminum (inner diameter 2.5 cm, height 6 cm) was designed to carry out in-situ freeze-drying experiments in the beamline. The particles were filled in precooled freeze-drying cells (for particle sizes and filling heights see Tab. 1) and the freeze-drying cells were connected to the sample stick as described in [4]. The pressure inside the freeze-drying cell was set to 10 Pa and controlled with a rotary vane pump and a controller (CVC3000, Vacuubrand, Germany). The pressure was measured with a pirani pressure sensor (VSP 3000, Vacuubrand, Germany).

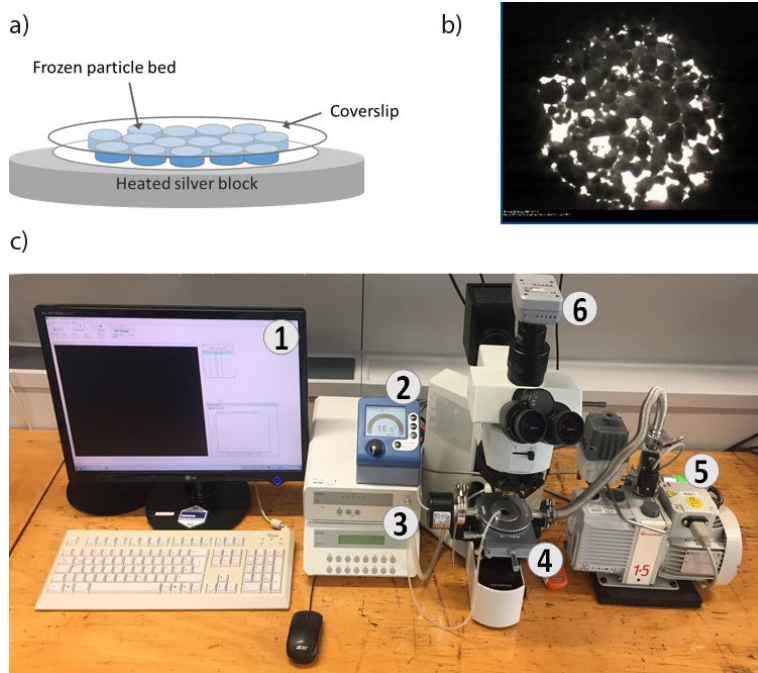


Figure 2. (a) Schematic picture of the sample and placement in the freeze-drying cell; (b) microscopic view of the sample; (c) setup of the lyomicroscope with (1) PC with Linksys software, (2) pressure control, (3) temperature control, (4) cool-stage under the light microscope, (5) rotary vane pump with control valve, (6) camera.

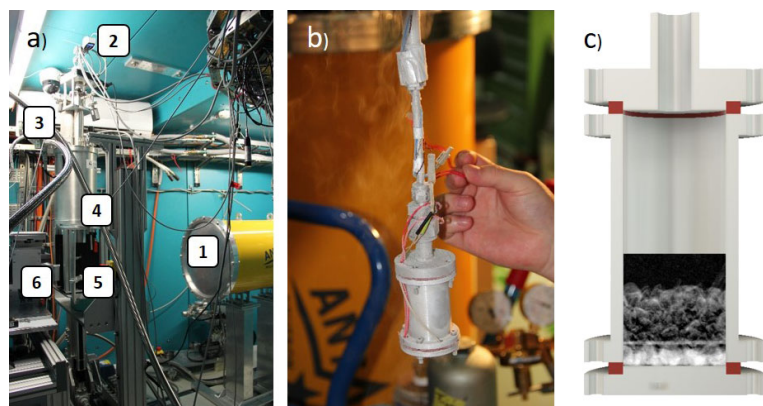


Figure 3. (a) Setup of the experiment. (1) Neutron beamline, (2) pressure sensor, (3) sample stick with rotation motor, (4) cryostat, (5) location of measurement cell, (6) scintillator. (b) Freeze-drying cell connected to sample stick, PT 1000 sensor, and heating foil. (c) Schematic view of region of interest inside the freeze-drying cell.

The bottom of the cell is equipped with a Kapton heating foil (Allectra GmbH, Germany) and the temperature of the bottom was set to -18°C . The temperature in the bottom of the cell was measured with a PT 1000 sensor (Innovative Sensor Technology, Switzerland) and controlled with a lakeshore controller. The walls of the freeze-drying cell are thermally insulated from the bottom by a silicon rubber seal (height 3 mm; Telle, Germany) from the bottom to prevent radial drying. The wall of the freeze-drying cell was cooled by a closed cycle cryostat to -42°C , which corresponds to the sublimation temperature of pure water at 10 Pa.

Radiographic images with a fixed sample position were taken every minute. The field of view in the setup had a width of 75.5 mm and a height of 89.5 mm. The maximum duration of the experiment was 26 h due to limitations in beamline access, i.e., all experiments were stopped before the end of primary drying. The exposure time was 2 s for the large particles with a $100\text{-}\mu\text{m}$ scintillator and 16 s for the small particles with a $50\text{-}\mu\text{m}$ scintillator. The experimental process conditions are listed in Tab. 1. Particle size refers to the mean particle size.

The image analysis and identification of the sublimation front is described in [4]. Briefly, the images (IM) at time t ($IM(t)$) that correspond to the relative transmission T' were corrected with the dark field image DF . The DF image is an

Table 1. Experimental conditions during the in situ freeze-drying experiments in neutron source at FRM II.

No.	Particle size [μm]	Conc. [-]	Bed height [mm]	Duration of experiment [h]
1	3550	0.05	14	15
2	3550	0.20	15	16
3	3550	0.05	25	21
4	3550	0.05	17	26
5	70	0.20	14	10
6	70	0.05	13	22

image taken without test setup and without neutron beam. To evaluate the sublimation front during the process, the image at time t ($IM(t)$) is related to the image at time t_0 at the start of the process.

$$T' = \frac{IM(t) - DF}{IM(t_0) - DF} \quad (1)$$

For neutron tomography, the cell was rotated by 180° by a rotation table and 700 projections were taken for reconstruction of the 3D image. To prevent further drying during tomographic measurements, the bottom of the freeze-drying cell was cooled to 225 K and the cryostat was cooled to 190 K until all projections were completed.

2.5 Estimation of Mass Transfer Coefficients and Drying Times

Effective diffusion coefficients inside single particles D_{in} as well as inner porosity of the particles ε_{in} can be estimated as described in [18]. In brief, freeze-dried particles were produced and the 3D pore structure was evaluated by X-ray microtomography. The images were analyzed by GeoDict (version 2017, Math2Market, Kaiserslautern) and effective diffusion coefficients were computed on the binarized images by a random walk method. It was shown that for freeze-drying of frozen sugar samples Knudsen diffusion is dominant [18].

For the calculation of the outer diffusion coefficients D_{out} in the packed bed, GeoDict (version 2017, Math2Market, Kaiserslautern) was also employed. For that, virtual packed particle beds from solid monodisperse particles were created by GrainDict (version 2017, Math2Market, Kaiserslautern). The outer porosity ε_{out} of the packed bed was also determined by GrainDict and is 0.42 ± 0.01 independent from the particle size. The effective outer diffusion coefficient through the packed bed was calculated for different particle sizes in the range between 20 and $5000\text{ }\mu\text{m}$. For Knudsen numbers $Kn > 1$, Knudsen diffusion was assumed as main diffusion mechanism. This was valid for all particle sizes up to $1000\text{ }\mu\text{m}$. For the particle sizes 2000 and $5000\text{ }\mu\text{m}$, the Bosanquet approximation (GeoDict version 2017, Math2Market, Kaiserslautern) was employed. As total outer mass transfer is composed of the contribution of diffusion and viscous flow, the total mass transfer coefficient is calculated according to as follows:

$$D_t = D_{out} + \frac{K}{\mu} p^* \quad (2)$$

Here D_t is the total outer mass transport coefficient, D_{out} the outer diffusion coefficient, K the Darcy permeability, μ the viscosity of water vapor, and p^* the saturation pressure. The Darcy permeability was calculated with the Carman-Kozeny correlation according to [19].

When the inner and outer effective diffusion coefficients as well as the porosities are known, the drying times can be calculated for the case that the process is fully mass transfer-

limited [18]. The drying time for a single particle with radius r in the bed is estimated according to:

$$t_{\text{particle}} = r^2 \frac{\varepsilon_{\text{in}} \rho_{\text{ice}} RT}{4M_{\text{W}} D_{\text{in}} p^*} \quad (3)$$

Here, ρ_{ice} is the density of the ice, T the temperature of the heated shelf, R the universal gas constant, M_{W} the molecular weight of water, and p^* the saturation pressure. In analogy to single spheres, the mass transport through the particle bed (only diffusion through outer pores is considered) with a given bed height h can be calculated with Eq. (4):

$$t_{\text{bed}} = h^2 \frac{\varepsilon_{\text{out}} \rho_{\text{ice}} RT}{2M_{\text{W}} D_{\text{t}}^*} \quad (4)$$

3 Results

3.1 Visualization of Drying Fronts in the Lyomicroscope

As already mentioned, the visualization of the drying front is only possible for thin slices which are cut out from packed bed (see Fig. 2). Depending on the chosen magnification, sublimation fronts inside the particles or in the bed could be observed. Fig. 4 illustrates the sublimation front inside a single maltodextrin

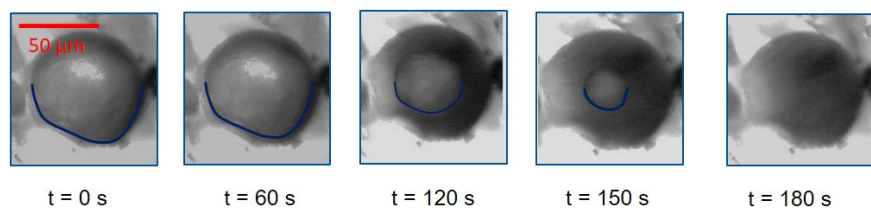


Figure 4. Sublimation front inside a maltodextrin particle ($x = 70 \mu\text{m}$, $c = 0.05$) at different time steps observed under the lyomicroscope ($T = -42^\circ\text{C}$; $p = 10 \text{ Pa}$). For better visualization, the drying front is marked with a blue line in the lower half of the circle.

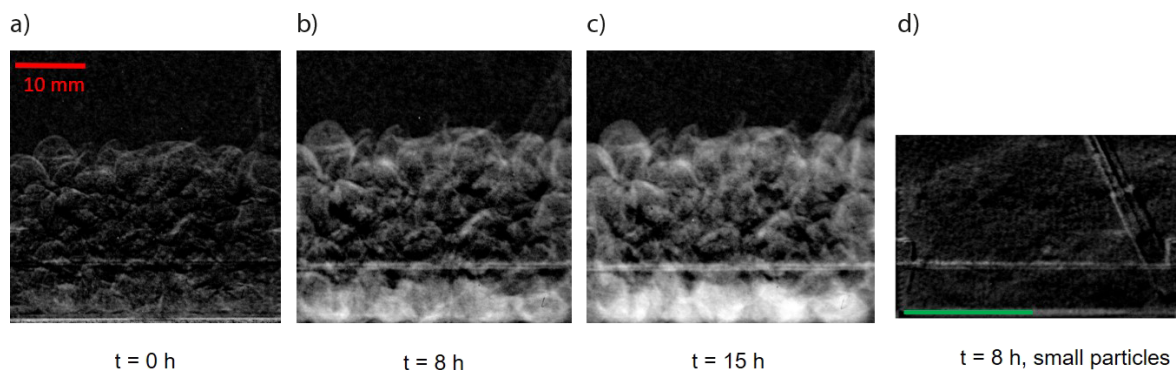


Figure 5. Neutron radiographic images after different drying times to show the evolution of the drying front for the large particle bed ($x = 3500 \mu\text{m}$, $c = 0.05$). (a) 0 h, (b) 8 h, (c) 15 h, (d) radiographic image after 8 h drying for small particles ($x = 70 \mu\text{m}$, $c = 0.05$). Images are transformed according to Eq. (1). Dry regions appear white, frozen regions and the background black. In the right picture, the dried area is indicated with a green line as the dried zone from the bottom is very tiny. Note that the bright horizontal lines in the images are an artefact and related to ice sublimation at the outside flange of the freeze-drying cell and therefore do not belong to the sublimation front of the particle bed (see [4, 17]). The position of the particles in the freeze-drying cell is depicted in Fig. 3c.

particle ($x = 70 \mu\text{m}$; $c = 0.05$). It is shown that intraparticle drying fronts are formed, visible by the radially growing darker area, and that drying of the particle is completed after 180 s. The sublimation fronts can be quantitatively evaluated and the particle-based drying kinetics extracted. It is found that larger particles have a longer drying time (data not shown). In addition to the sublimation front inside the particles, a front through the bed is also detected. As this front is quite blurred, it is so far not possible to quantitatively evaluate this front.

3.2 Visualization of Drying Fronts with Neutron Imaging

With neutron imaging, it is possible to detect local changes in water content [4]. The change in relative gray values (Eq. (1)) is related to a change in water content. Brighter regions inside the particle bed refer to drier regions, relative to the initial image. In order to investigate exemplarily the impact of the particle size, two different particle sizes (70 and $3550 \mu\text{m}$, see Tab. 1) were chosen to achieve different outer pore sizes in the bed. Furthermore, two different solid concentrations were employed to achieve different inner pore sizes [18]. By choosing combinations of these parameters, the ratio of inner to outer pore size can be varied.

Figs. 5a–c present a time series of radiographic images of the sublimation front in the large particle bed with low maltodextrin concentration ($c = 0.05$). In comparison, the radiographic image after 8 h drying for the small particles is given in Fig. 5d.

The time series in Fig. 5 shows a sublimation front for large particles evolving from the bottom to the top of the bed indicated by the brighter region close to the bottom of the bed. This confirms the model developed in [8]. Besides the main sublimation front, is

also visible that the gray value decreases throughout the particle bed. This means that sublimation occurs at multiple locations in the bed. This gives a hint on intraparticle sublimation fronts as suggested by [6].

For the small particles in the image in Fig. 5d, only a very tiny dry area (brighter region) becomes visible at the bottom of the bed, also showing a sublimation direction from the bottom to the top of the bed. This means that the sublimation of fine particles is proceeding much slower than the sublimation of large particles. Furthermore, the gray value outside the main sublimation front seems to decrease less strongly than for the bed of large particles, suggesting that radial sublimation fronts inside the particles are less pronounced.

To validate the evolution of multiple sublimation fronts inside the single particles, tomographic measurements were carried out for the large particles to get the full 3D information. The tomographic reconstruction in the equatorial plane of the lowest layer of particles is illustrated in Fig. 6. This figure demonstrates the evolution of the drying front in the equatorial plane of the lowest particle layer and confirms the assumption that radial fronts are evolving in each particle. This is visible as the decrease of the frozen area (light gray) over drying time. This result supports the model suggested by Trelea et al. [6] for large particles and supports the hypothesis that for the large particles, the main resistance to mass transfer lies within the particles. For small particles, intraparticle sublimation fronts could not be observed due to insufficient resolution of the scintillator.

3.3 Estimation of the Biot Number

To estimate whether the inner or outer mass transfer resistance is dominating, a modified Biot number is introduced which includes the particle size x , the bed height h , the outer total mass transfer coefficient D_t , and the effective diffusion coefficient D_{in} inside the particle. As both D_t and D_{in} are influenced by the porosity, the pore size, and the tortuosity, the modified Biot number also includes the influence of inner to outer pore size ratio. The modified Biot number is defined as:

$$Bi_m = \frac{D_t x^2}{D_{in} h^2} \quad (5)$$

Large Bi_m numbers ($Bi_m \gg 1$) mean that the mass transfer process is mainly limited inside the particle, which is the case in the model of Trelea et al. [6]. Small Bi_m numbers ($Bi_m \ll 1$) indicate that the mass transfer process is mainly limited in the bulk, and the mass transfer resistance inside the particles can be neglected. This means that depending on the bed height and the ratio of the inner to outer mass transfer coefficient there exists a limiting particle size where the mass transfer resis-

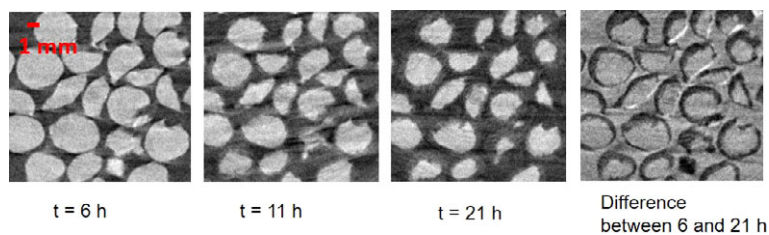


Figure 6. Cross section of tomographic reconstruction of the equatorial plane of the particle layer at the bottom of the bed showing the evolution of radial intraparticle drying fronts after different drying times ($c = 0.05$, $d = 3500 \mu\text{m}$). Light gray: frozen area; medium gray: dried part; dark gray: voids. For better visualization of drying fronts, the difference between the first and third picture was calculated with imageJ (version 1.52a, NIH, USA).

tance transforms from internally to externally controlled. $Bi = 1$ indicates that the stationary diffusion time for the radial diffusion through the particle is in the same time scale as the mass transfer through the bed. The modified Biot number can therefore be used (i) to identify suitable particle size for a given bed height and (ii) to identify the most suitable model for freeze-drying of bulky solids. The modified Biot number for different particle sizes was calculated for the given bed heights with the inner and outer mass transport coefficients. The outer mass transport coefficient was calculated as described in Sect. 2.5. The inner mass transport coefficient was taken from [18]. Fig. 7 shows the dependence of the modified Biot number for two different bed heights and solid concentrations on the particle size.

To demonstrate the impact of particle size on the total drying time under the assumption of stationary mass transfer and under mass transfer-limiting conditions, the primary drying time is plotted as a function of particle size (Fig. 8). The primary drying times for the two limiting cases was calculated

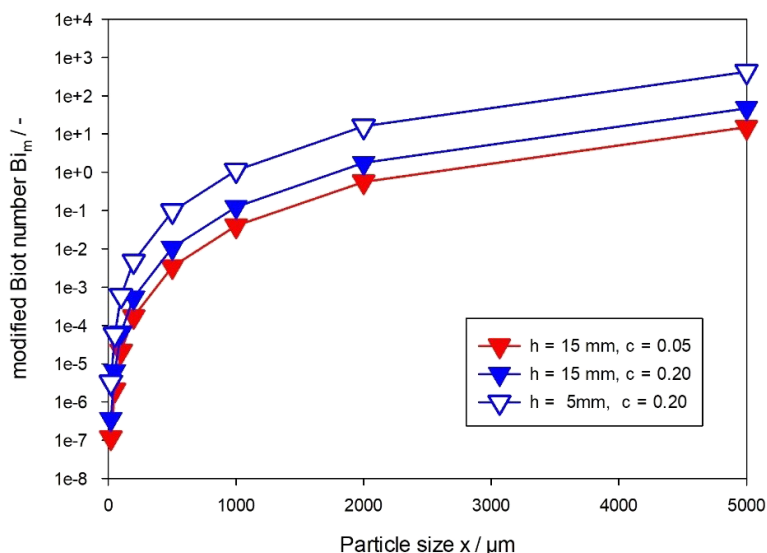


Figure 7. Calculated modified Biot number Bi_m for the mass transfer in maltodextrin particles as a function of particle size for two different formulations ($c = 0.05$ and 0.2) and two different bed heights ($h = 5$ and 15 mm).

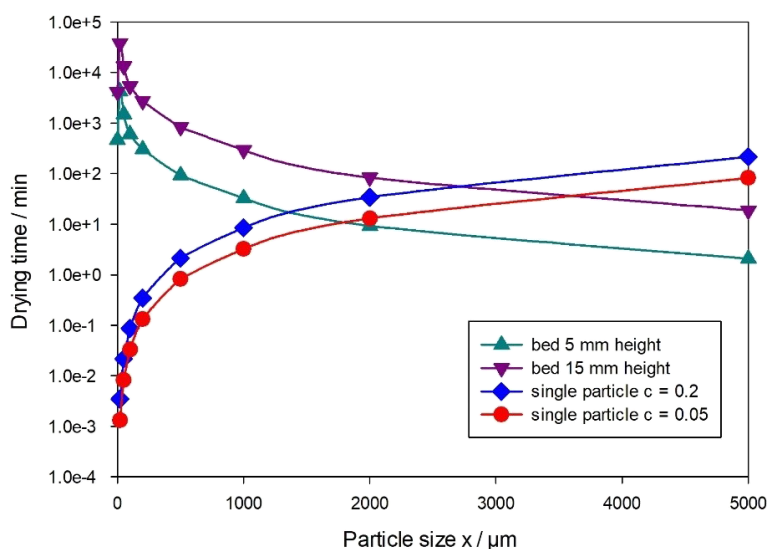


Figure 8. Calculated primary drying time (Eqs. (3) and (4)) for maltodextrin particles and particle beds under the assumption of stationary mass transfer for particle beds with two different heights ($h = 5$ and 15 mm) and for single particles of two different formulations ($c = 0.05$ und 0.2).

according to Eqs. (3) and (4). It is shown that for very small particles, such as employed in spray freeze-drying in the pharmaceutical industry, the drying time is longer compared to compact solutions due to the expanded bulk volume and therefore bed height. For particle beds, the drying time decreases with increasing particle size and reaches the level of the compact solution again at a particle size $x > 100 \mu\text{m}$. On a single particle level, the drying time increases with larger particle size. The minimum possible drying time is given by the intercept of the single particle curve with the curve for the packed bed. The intercept depends on the bed height and the solid concentration in the particle which determines the pore size.

4 Summary and Discussion

Two methods have been introduced to investigate sublimation fronts during freeze-drying of bulky solids. Both methods are suitable to visualize sublimation fronts but they have different limitations.

4.1 Lyomicroscopy

In lyomicroscopy, sublimation fronts can mainly be visualized on a particle scale. For that, a slice of the frozen packed bed has to be prepared by a microtome. Depending on the magnification, also pore-scale effects on the sublimation front can be studied. However, quantification of sublimation fronts in the particle bed is difficult. Therefore, lyomicroscopy is most advantageous for the study of the sublimation front on a particle and pore scale level, e.g., for the purpose to develop and validate pore network models [20]. Furthermore, due to the miniaturized setup of the cool-stage, the sample diameter is less than 5 mm which means that maximum bed dimensions are

limited and fixed leading to higher Bi_m numbers. In addition, the maximum particle size in the bed is also limited to a few hundred microns. In lyomicroscopy, the bed height of the particle bed refers to the radius of the sliced sample (see Fig. 2). Another aspect of the investigation of sublimation fronts in lyomicroscopy is that due to the 2D setup and the investigation in a thin slice of sample, the drying process is mass transfer-limited [18]. Therefore, it is possible to determine intraparticle diffusion coefficients [12].

4.2 Neutron Imaging

Due to the high sensitivity of neutrons to hydrogen, neutron imaging is considered to be a very suitable technique to visualize sublimation fronts in situ in packed particle beds [4]. With neutron radiography, only the main sublimation front can be studied in a broad range of particle sizes (see Fig. 5). With neutron tomography, it is also possible to study particle-based sublimation fronts three-dimensionally for the large particles (see Fig. 6).

However, the process has to be stopped for tomographic evaluation. Therefore, for large particles, neutron imaging is appropriate for both the investigation of sublimation fronts inside particles and through the packed particle bed. For small particles, only sublimation fronts through the bed can be visualized with neutron radiography with the current resolution.

The investigation with neutron imaging is possible on a larger scale under real process conditions, i.e., coupled heat and mass transfer, and a larger range of particle sizes and bed heights as compared to the lyomicroscope. Therefore, a broad range of Biot numbers can be achieved. This makes neutron imaging a powerful technique to study freeze-drying processes of bulk solids. However, as the neutron imaging experiments are bound to large-scale research facilities, the available beam time is restricted and care has to be taken to identify the most interesting process conditions and best preparation and planning is needed to get the most out of the experiments.

It has to be noted that for particle beds – in contradiction to frozen solutions – the process is often heat transfer-limited due to the decrease of thermal conductivity with increasing porosity and the fact that a dry insulating layer occurs at the heated bottom of the freeze drier (see Fig. 5) [6, 8]. Therefore, in a further step, the considerations made here for the mass transfer have to be extended to the heat transfer to (i) identify an optimum particle size and bed height depending on the formulation and (ii) to identify the most suitable model for modeling freeze-drying of bulky solids.

Acknowledgment

This work is based on experiments performed at the ANTARES instrument operated by FRMII at the Heinz Maier-Leibnitz Zentrum (MLZ), Garching, Germany. The authors would like to thank Christian Hansen A/S for providing the freeze-drying

microscope. The help of Katharina Hiller with the lyomicroscopic measurements and Seongshik Kim with the computation of diffusion coefficients is gratefully acknowledged.

The authors have declared no conflict of interest.

Symbols used

Bi_m	[-]	modified Biot number
c	[-]	concentration
D	[m ² s ⁻¹]	effective diffusion coefficient
DF	[-]	dark field
h	[m]	bed height
IM	[-]	image
K	[m ²]	Darcy permeability
Kn	[-]	Knudsen number
M	[kg mol ⁻¹]	molecular weight
\dot{M}_{sub}	[kg h ⁻¹]	sublimed water vapor
p	[Pa]	pressure
p^*	[Pa]	saturation pressure
\dot{Q}_{heat}	[W]	heat flow provided by the lower plate
r	[m]	radius
R	[J mol ⁻¹ K ⁻¹]	universal gas constant
s	[m]	thickness of dry layer
t	[s]	time
t_0	[s]	time at the start of the process
$t_{particle}$	[s]	drying time for a single particle
T	[K]	shelf temperature
T'	[-]	relative transmission
T'_g	[K]	temperature of the maximally freeze-concentrated solution
T_{heat}	[K]	temperature of the heating plate
T_{sub}	[K]	temperature at the sublimation front
x	[m]	particle size
x_{pm}	[m]	equivalent diameter

Greek letters

ε	[-]	porosity
μ	[Pa s]	viscosity
ρ	[kg m ⁻³]	density

Sub- and superscripts

in	inner
out	outer
t	total
W	water

References

- [1] A. Arsiccio, A. C. Sparavigna, R. Pisano, A. A. Barresi, *Drying Technol.* **2019**, *37* (4), 435–447. DOI: <https://doi.org/10.1080/07373937.2018.1430042>

- [2] R. Pisano, A. Arsiccio, K. Nakagawa, A. A. Barresi, *Drying Technol.* **2019**, *37* (5), 579–599. DOI: <https://doi.org/10.1080/07373937.2018.1528451>
- [3] K. Nakagawa, S. Tamiya, *AIChE J.* **2019**, *65* (5), e16571. DOI: <https://doi.org/10.1002/aic.16571>
- [4] S. Gruber, N. Vorhauer, M. Schulz, M. Hilmer, J. Peters, E. Tsotsas, P. Foerst, *Chem. Eng. Sci.* **2020**, *2020* (211), 115268.
- [5] *Freeze-Drying* (Eds: G. Oetjen, P. Haseley), Vol. 2, Wiley-VCH, Weinheim **2003**.
- [6] I. C. Trelea, S. Passot, M. Marin, F. Fonseca, *J. Biomech. Eng.* **2009**, *131* (7), 074501. DOI: <https://doi.org/10.1115/1.3142975>
- [7] A. I. Liapis, R. Bruttini, *Int. J. Heat Mass Transfer* **2009**, *52* (1), 100–111. DOI: <https://doi.org/10.1016/j.ijheatmasstransfer.2008.06.026>
- [8] T. Chitu, S. Vessot, R. Peczkalski, J. Andrieu, B. Woinet, A. Françon, *Drying Technol.* **2015**, *33* (15–16), 1892–1898. DOI: <https://doi.org/10.1080/07373937.2015.1066386>
- [9] P. Foerst, S. Gruber, M. Hilmer, N. Vorhauer, M. Schulz, E. Tsotsas, *Proc. of EuroDrying'2019*, Politecnico di Torino, Torino **2019**.
- [10] P. Raman, C. D. Rielly, A. G. F. Stapley, *Proc. of the 19th Int. Drying Symp. (IDS 2014)*, EDP Sciences, Les Ulis, France **2014**.
- [11] P. Ray, C. D. Rielly, A. G. F. Stapley, *Chem. Eng. Sci.* **2017**, *172*, 731–743. DOI: <https://doi.org/10.1016/j.ces.2017.05.047>
- [12] S. Zhai, R. Taylor, R. Sanches, N. K. H. Slater, *Chem. Eng. Sci.* **2003**, *58* (11), 2313–2323. DOI: [https://doi.org/10.1016/S0009-2509\(03\)00090-3](https://doi.org/10.1016/S0009-2509(03)00090-3)
- [13] T. Defraeye, W. Aregawi, S. Saneinejad, P. Vontobel, E. Lehmann, J. Carmeliet, P. Verboven, D. Derome, B. Nicolai, *Food Bioprocess Technol.* **2013**, *6* (12), 3353–3367. DOI: <https://doi.org/10.1007/s11947-012-0999-y>
- [14] T. Defraeye, B. Nicolai, D. Mannes, W. Aregawi, P. Verboven, D. Derome, *J. Food Eng.* **2016**, *178*, 198–202. DOI: <https://doi.org/10.1016/j.jfoodeng.2016.01.023>
- [15] M. Schulz, B. Schillinger, *J. Large-Scale Res. Facil.* **2015**, *1*, A17. DOI: <https://doi.org/10.17815/jlsrf-1-42>
- [16] E. Calzada, F. Gruenauer, M. Mühlbauer, B. Schillinger, M. Schulz, *Nucl. Instrum. Methods Phys. Res., Sect. A* **2009**, *605* (1–2), 50–53. DOI: <https://doi.org/10.1016/j.nima.2009.01.192>
- [17] M. Hilmer, J. Peters, M. Schulz, S. Gruber, N. Vorhauer, E. Tsotsas, P. Foerst, *J. Sci. Instrum.* **2020**, *91*, 014102. DOI: <https://doi.org/10.1063/1.5126927>
- [18] P. Foerst, T. Melo de Carvalho, M. Lechner, T. Kovacevic, S. Kim, C. Kirse, H. Briesen, *J. Food Eng.* **2019**, *260*, 50–57. DOI: <https://doi.org/10.1016/j.jfoodeng.2019.05.002>
- [19] C.-S. Song, G.-S. Yeom, *Heat Mass Transfer* **2009**, *46* (1), 39. DOI: <https://doi.org/10.1007/s00231-009-0542-5>
- [20] N. Vorhauer, P. Foerst, H. Schuchmann, E. Tsotsas, *Proc. IDS'2018: 21st Int. Drying Symp.*, Editorial Universitat Politècnica de València, València **2018**.